

PAPER

ASMADA—A tool for automatic analysis of shape memory alloy thermal cycling data under constant stress

To cite this article: Matthew C Kuner *et al* 2021 *Smart Mater. Struct.* **30** 125003

View the [article online](#) for updates and enhancements.

You may also like

- [Impact damage resistance and damage suppression properties of shape memory alloys in hybrid composites—a review](#)
S L Angioni, M Meo and A Foreman
- [Shape memory alloy torsional actuators: a review of applications, experimental investigations, modeling, and design](#)
H Stroud and D Hartl
- [A review of modeling techniques for advanced effects in shape memory alloy behavior](#)
Cheikh Cisse, Wael Zaki and Tarak Ben Zineb

ASMADA—A tool for automatic analysis of shape memory alloy thermal cycling data under constant stress

Matthew C Kuner^{*} , Anargyros A Karakalas^{*} 
and Dimitris C Lagoudas 

Department of Aerospace Engineering, Texas A&M University, College Station, TX,
United States of America

E-mail: matthewkuner@gatech.edu and karakalas@tamu.edu

Received 4 May 2021, revised 6 September 2021

Accepted for publication 7 October 2021

Published 25 October 2021



Abstract

The authors present the automatic shape memory alloy data analyzer (ASMADA). ASMADA is capable of rapid, robust, and consistent processing of shape memory alloy thermal cycling data acquired under constant stress. This seeks to address two primary issues: the lack of unified analysis procedures in relevant standards and the near-universal manual analysis of such data. ASMADA is compliant with the definitions provided in ASTM standards and calculates up to twenty-three (23) material properties/parameters at speeds ranging from 5 to 35 cycles s^{-1} . These parameters include the four transformation start/finish temperature thresholds, which are calculated using the tangent line method; the transformation region tangent lines are determined using a modified sigmoid function, whereas the single-phase region tangent lines are determined based on the geometry of the cycle data. Additionally, a graphical user interface is provided to make the tool readily accessible and easy to navigate. The capabilities of ASMADA have been tested on experimental data from four different research groups; results from five of these tests are presented to demonstrate the tool's robustness. This tool was developed in Python and is publicly available at <https://github.com/matthewkuner/ASMADA>

Supplementary material for this article is available [online](#)

Keywords: shape memory alloys, thermal cycling, analysis methodology, automatic data analysis, actuation fatigue, open-source python tool

(Some figures may appear in colour only in the online journal)

1. Introduction

Shape memory alloys (SMAs) are a unique class of metals that can remember and return to their previous shape after being inelastically deformed. The crystal structure of SMA is known to obtain two primary phases: Austenite (A), which has higher symmetry and is formed at higher temperatures, and Martensite (M), which has lower symmetry and is formed at lower temperatures. The ability to 'remember' a previous

shape stems from a reversible, diffusion-less, solid-state phase transformation between Austenite and Martensite. This can be induced by the application of heat and/or stress, while a sequential loading path where thermal and mechanical loads take place may result in what is called the 'shape memory effect'.

Due to their characteristics, SMA have seen application in aerospace [1, 2], biomedical [3], automotive [4, 5], and oil and gas industries [6]. Quite recently, SMA have been considered as actuation elements for morphing of large wind turbine blades in order to enable active load alleviation [7, 8]. In the aerospace field, SMA can replace conventional actuators, such

^{*} Authors to whom any correspondence should be addressed.

as hydraulic pistons or servo-motors, due to their compactness, simplicity, and high energy density [9]. One example of such an application is in variable geometry chevrons, where SMA are activated to change the geometry of a jet engine outlet to significantly reduce noise upon takeoff and landing [10, 11].

Regardless of the application field, the experimentally observed non-linear, hysteretic, temperature- and stress-dependent behavior of SMA is evident in almost all physical properties of these materials. Young's modulus, hardness, coefficient of thermal expansion, thermal resistivity, and electrical resistivity are only a few of the properties that obtain different values between the two pure phases and thus change through transformation. Consequently, proper description of these property changes was deemed essential from the early stages of SMA research. The most widely adopted approach is their association with four key temperature thresholds that indicate the onset and the completion of the 'forward' ($A \rightarrow M$) and the 'reverse' transformation ($M \rightarrow A$) [10, 12, 13]. The most common practice followed for the determination of these thresholds is the realization of thermal cycles under constant mechanical load (iso-stress thermal cycling—ITC). The temperature range is most often selected to induce a complete phase transformation when characterizing a material's behavior [14], however, partial cycling is also not uncommon. Outside of material characterization, ITC is an experimental process regularly adopted for 'training', i.e. stabilization of material behavior [15–17], determination of actuation fatigue life [18–21], and last but not least calibration of a wide range of constitutive models [22–24].

All of the previously mentioned experimental processes require that more than one thermal cycle is performed. For the purposes of material characterization and calibration of constitutive models, usually a few cycles (~ 3 to 10) performed under slow cooling and heating rates suffice. In contrast, the experiments that are conducted to train the material or investigate its actuation fatigue life require a number of cycles that is orders of magnitude higher while they might be realized at a wide range of loading/unloading rates. A training process usually requires between 60 and 120 cycles (depending on the alloy composition, material processing, etc), while actuation fatigue experiments may require thousands or tens of thousands of cycles performed at high cooling and heating rates [25, 26].

Although a specific standard of high importance has been established for the determination of critical transformation temperature thresholds and other related metrics [27], this mainly provides the definitions of the most important/key properties that should be considered to characterize the material. In this generic framework, the available guidelines establish a consensus on the methodology only at a high level; no consideration is given for any implementation details applicable to real experimental data that might include noise or be collected using a wide range of measurement techniques. To this end, there is a necessity for developing tools that would complement the standardized testing and post-processing information allowing for consistent implementation.

Today, data from ITC tests almost universally undergo manual analysis that requires visual inspection and tangent line fitting [28–33] (similar to the analysis of differential scanning calorimetry data often used for SMA [34–36]). The most significant downsides of manual analysis are (a) the long processing time and (b) the introduction of human error due to subjectivity. The former is especially detrimental for actuation fatigue data, as it is not practically feasible to manually analyze large numbers of cycles, while the latter affects the accuracy and the consistency of the determined metrics. These obstacles force researchers to either: (a) manually analyze a small number of selected cycles, or (b) willingly choose to not calculate several key material properties from their data. To accelerate the process, researchers may develop custom, in-house post-processing codes for filtering, analyzing and extracting data, yet such approaches are mostly developed considering the capabilities of the equipment used to acquire the data, their output format, specific test protocols followed, etc. Such considerations may limit the applicability of the developed approaches to a wider variety of data sets. Furthermore, discrepancies in the analysis methods used by different researchers around the globe make the direct comparison of their results less meaningful.

It is important to note that practically identical methods are used for analyzing ITC data collected for the purposes of material training [37], characterization [38, 39], determination of two-way shape memory effect (TWSME) [40], calibration of constitutive models [41], monitoring the evolution of material behavior in crack growth studies [21], and functional fatigue life determination [42], despite the fact that these tests serve different purposes. Thus, it is possible for a single tool to properly analyze data from all forms of ITC tests and extract material properties/parameters and their evolution across thermal cycles, which can be leveraged for the development of models able to account for the complex behavior of SMA. Furthermore, the methodology proposed in this work for the automatic analysis of the ITC data and the extraction of quantities related with SMA behavioral aspects can be applied to both conventional SMA materials systems as well as high temperature shape memory alloys (HTSMAs), like NiTiHf [43–45], as well as high entropy SMA that have recently presented vivid research interest [46–49]. Finally, this approach can also be adopted for the analysis of the transformation characteristics of SMA actuators when subjected to stochastic/variable magnitude activation cycles [9] as well as the comparative analysis of different SMA actuators or actuator configurations [50].

In this work, the authors present the 'automatic shape memory alloy data analyzer' (ASMADA). ASMADA is a robust tool for SMAs with the capability to automatically analyze thermal cycling test data obtained under constant mechanical loading. Developed in Python so that it can be made publicly available to the research community, ASMADA calculates a total of twenty-three (23) different material properties and parameters using methods compliant with ASTM standard E-3097-17 [27]. A 'graphical user interface' (GUI) has been created to complement this functionality by allowing

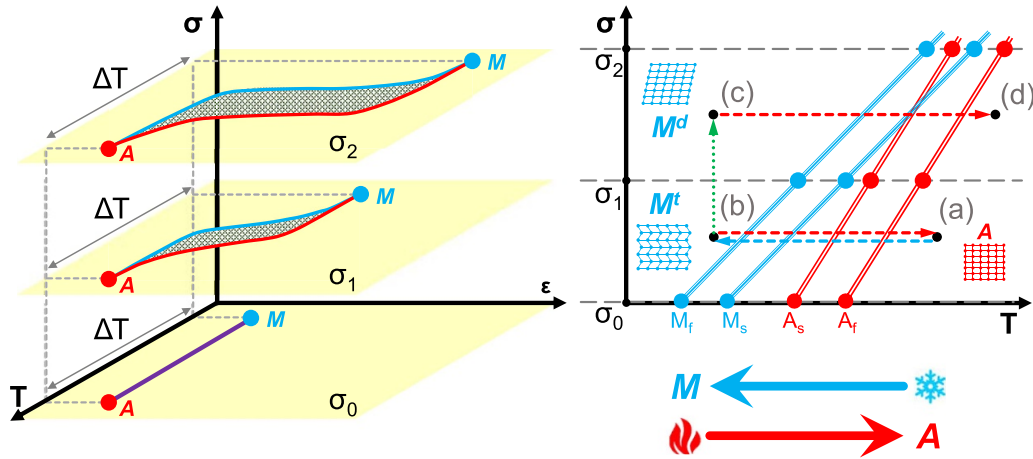


Figure 1. Graphic representation of phase diagram drawing process.

different researchers to easily analyze their data regardless of file formatting. Finally, the robustness of this tool was tested using thermal cycling data from five researchers working in four different research groups within the field of SMA.

The paper is structured as follows. Section 2 provides background and theory for the phase transformation mechanisms of interest, as well as the definitions of the metrics used to quantify these mechanisms. Section 3 describes the proposed methodology used to calculate these metrics from experimental data, including the GUI structure. Section 4 presents the results from an example experimental test (with additional results presented in the supplementary materials (available online at stacks.iop.org/SMS/30/125003/mmedia)), alongside details of the advantages and limitations of ASMADA and areas of future work. Finally, the work is summarized in section 5.

2. Thermal cycling of SMA under constant mechanical load

2.1. SMA characteristics

As mentioned in section 1, the crystal structures of SMA are able to undergo a diffusion-less, solid-state transformation that is attributed to the distortion of crystal lattice under shear. Under absence of mechanical load, the high temperature, parent phase of Austenite can be fully transformed to the lower temperature, product phase of Martensite by cooling the material below a critical temperature threshold, which is denoted as M_f (thermal loading path indicated from point (a) to point (b) in figure 1). This transition from Austenite to the ‘Twinned’, or so-called ‘self-accommodated’ Martensite, is performed without the production of any associated strain since, according to Bhattacharya [51], the arrangement of Martensitic variants occupies a region whose boundary suffers no displacement with respect to Austenite. If the Twinned Martensitic phase is heated above a critical temperature threshold, denoted as A_f , the material will return back to its original Austenitic phase (path indicated from point (b) to point (a) in figure 1). However, should mechanical load be

applied while in the Twinned Martensitic state, the Martensite will de-twin and a less-symmetric ‘Detwinned’ Martensitic phase will be formed (mechanical loading path from point (b) to point (c)). This crystal deformation is accompanied by an inelastic strain that remains even if the mechanical load is removed. This inelastic strain is called ‘transformation strain’ and is commonly represented as ϵ_t . Yet, the material is able to return back to the original Austenitic phase and recover this transformation strain by heating it above the Austenitic finish temperature (A_f) (from point (c) to point (d)). At this point, it is important to mention that Austenite may reach a fully Detwinned Martensitic state and produce a transformation strain directly through cooling (transition from point (d) back to point (c) in the schematic of figure 1). However, a mechanical stimulus that exceeds a critical stress level has to be applied before any temperature change is attempted.

Assuming a constant stress level, a given temperature variation, between an upper cycle temperature (UCT) and a lower cycle temperature (LCT), results in the realization of a complete transition from Austenite to Martensite and back—thus, a hysteresis loop is formed, like the one shown schematically for two different stress levels in the left diagram of figure 1. The hysteresis branch closer to the temperature axis (blue) represents the response when the forward transformation takes place, while the other hysteresis branch (red) is formed during the reverse transformation. It is important to note that both transformation directions are accompanied by either the production or the absorption of heat since they are associated with exothermic and endothermic processes, respectively. Thus, the difference between the areas under these two curves determines the hysteresis loop area and is associated with the energy dissipated due to the transformation cycle.

Repeated thermal cycling can lead to the production of residual strains, denoted as ϵ_{res} in figure 2. Part of the residual strain is attributed to the mismatch between the Austenitic and Martensitic thermal strains. Yet, the major constituents of ϵ_{res} may include transformation induced plasticity (TRIP), viscoplastic or any other types of permanent or evolving strains that accumulate as the number of cycles increases. An example of subsequent thermal cycles which induce evolving residual

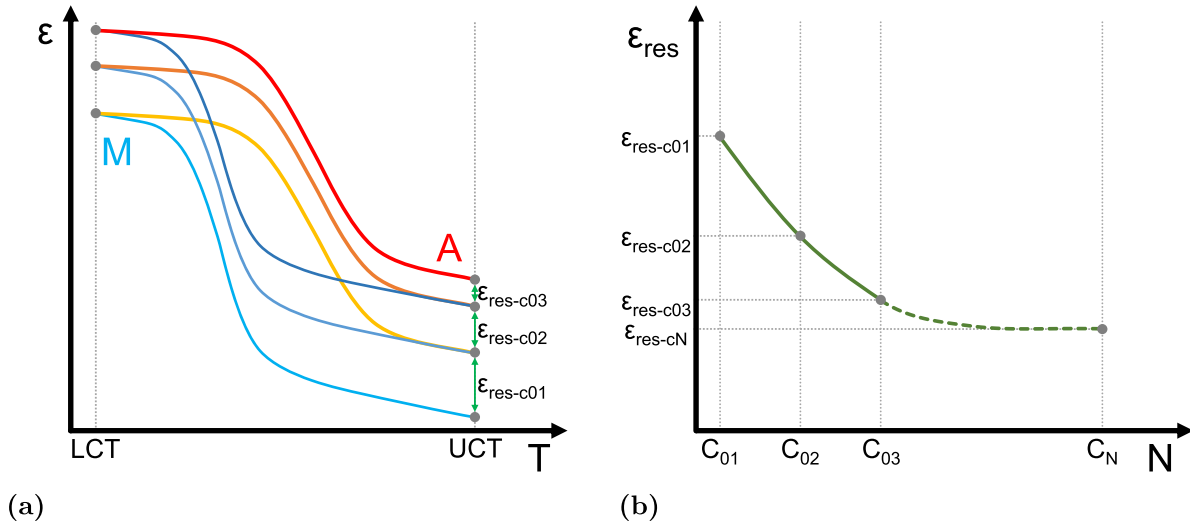


Figure 2. Typical evolution of residual strains in (a) the strain vs. temperature plain and (b) residual strain vs. number of thermal cycles.

strain is presented in figure 2; the case shown is quite typical, with an accumulation of TRIP strains that evolve and saturate after some number of cycles.

2.2. ASTM-based definitions for calculating material properties

Appropriate methods for determining material properties from ITC experimental data are contained within ASTM standard E-3097-17 [27], and will be described here.

Idealized data from a single cycle of an ITC test is presented in figure 3. As shown, a constant stress level and a given temperature variation, between a UCT and an LCT, results in the realization of a complete transition from Austenite to Martensite and back. The pure phase of Austenite is present at higher temperatures and lower absolute strain, whereas Martensite is present at lower temperatures and higher absolute strain. Note that the steeper regions indicate that a phase transformation is actively occurring, whereas the flatter regions indicate that the transformation is complete and only one phase is present.

Key properties to measure include the two pairs of start and finish points of these transformations, which describe the temperature and strain under which an SMA material's reversible $A \leftrightarrow M$ transformation is triggered. Referring to figure 3 and ASTM F2005-05 [52], M_s indicates the start of the forward transformation. M_f denotes that the sample is in the fully Martensitic phase. A_s indicates that the material is beginning to transition back into Austenite. Lastly, A_f indicates that the pure phase of Austenite has been obtained once again. To calculate the four properties, the accepted method involves finding the intersection of two tangent lines: one from the relevant single-phase region and one from the steeper transformation region. It is worth noting that these parameters are dependent on the transformation direction, i.e. values often differ for the $A \rightarrow M$ relative to the $M \rightarrow A$ transformation.

A complete list of properties and parameters, alongside the methods used to calculate them, is shown in table 1.

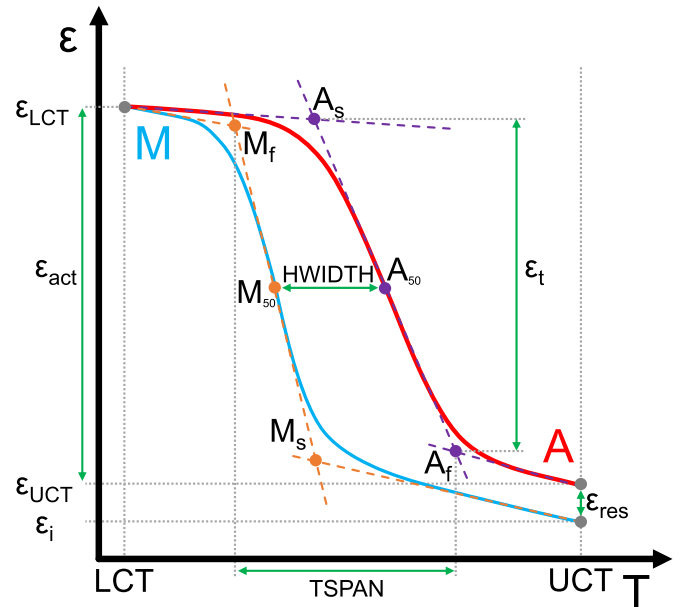


Figure 3. Terminology based on ASTM E-3097-17.

All of these properties are determined by the proposed tool.

3. Developed methodology

In this section, the developed methodology that is implemented in ASMADA is discussed in detail. A flowchart of the process employed is depicted in figure 4. For simplicity, this flowchart pertains only to the determination of transformation start/finish points.

3.1. Graphical user interface

It is expected that different researchers store their raw experimental data in a wide range of formats. Hence, the first step of

Table 1. Definitions of properties and parameters calculated.

Property/parameter	Symbol	Definition and determination approach
Martensite start temperature	M_s	Temperature threshold indicating the initiation of the forward transformation. Determined by the intersection of the appropriate tangent lines.
Martensite finish temperature	M_f	Temperature threshold indicating the completion of the forward transformation. Determined by the intersection of the appropriate tangent lines.
Austenite start temperature	A_s	Temperature threshold indicating the initiation of the reverse transformation. Determined by the intersection of the appropriate tangent lines.
Austenite finish temperature	A_f	Temperature threshold indicating the completion of the reverse transformation. Determined by the intersection of the appropriate tangent lines.
Martensite start strain	εM_s	Strain corresponding to the M_s temperature. Determined by the intersection of the appropriate tangent lines.
Martensite finish strain	εM_f	Strain corresponding to the M_f temperature. Determined by the intersection of the appropriate tangent lines.
Austenite start strain	εA_s	Strain corresponding to the A_s temperature. Determined by the intersection of the appropriate tangent lines.
Austenite finish strain	εA_f	Strain corresponding to the A_f temperature. Determined by the intersection of the appropriate tangent lines.
Lower cycle temperature	LCT	Minimum temperature within a cycle.
Upper cycle temperature	UCT	Maximum temperature within a cycle.
Strain at lower cycle temperature	ε_{LCT}	Strain corresponding to the LCT data point.
Strain at upper cycle temperature	ε_{UCT}	Strain corresponding to the UCT data point.
Initial strain	ε_i	Ordinate of the first data point of the cycle, i.e. immediately before cooling.
Residual strain	ε_{res}	Amount of permanent, inelastic strain developed during a given cycle. Calculated as per: $\varepsilon_{res} = \varepsilon_{UCT} - \varepsilon_i$.
Actuation strain	ε_{act}	Strain recovered when heating from the LCT to the UCT. Calculated as per: $\varepsilon_{act} = \varepsilon_{LCT} - \varepsilon_{UCT}$.
Transformation strain	ε_t	Strain recovered as a result of the reverse transformation. Calculated as per: $\varepsilon_t = \varepsilon_{A_s} - \varepsilon_{A_f}$.
*50% Austenite temperature	A_{50}	Temperature corresponding to 50% completion of the reverse transformation. Calculated as per: $A_{50} = \frac{A_s + A_f}{2}$.
*50% Martensite temperature	M_{50}	Temperature corresponding to 50% completion of the forward transformation. Calculated as per: $M_{50} = \frac{M_s + M_f}{2}$.
**Hysteresis area	HAREA	Area enclosed between a cycle's two thermal hysteresis branches. Calculated as per: $HAREA = \text{Area}_{\text{heating}} - \text{Area}_{\text{cooling}} $.
Hysteresis width	HWIDTH	Width of the thermal hysteresis. Calculated as per: $HWIDTH = A_{50} - M_{50}$.
Thermal transformation span	TSPAN	Temperature range between the A_f temperature and the M_f temperature. Calculated as per: $TSPAN = A_f - M_f$.
Coefficient of thermal expansion of Austenite	α^A	Slope of the pure Austenitic phase region.
Coefficient of thermal expansion of Martensite	α^M	Slope of the pure Martensitic phase region.
**Minimum cycle strain	$\varepsilon_{\text{cycle-min}}$	Minimum strain within a cycle.
**Maximum cycle strain	$\varepsilon_{\text{cycle-max}}$	Maximum strain within a cycle.

* Intermediate property/parameter not outputted by ASMADA.

** Property/parameter is *not* defined within any ASTM standards known to the authors.

analysis involves the user specifying how their experimental data should be interpreted. To make this process easier, a GUI was developed. The main window of this interface is shown in figure 5.

The latest version of the GUI offers several features, the most important of which are outlined below:

- the user may select a data file for analysis by clicking on button 'A1' and navigating to the file location. Once selected, the file name and format extension will be displayed in field 'A2'. The GUI then automatically loads some of the data contained in the file and previews them in the table shown on the right.

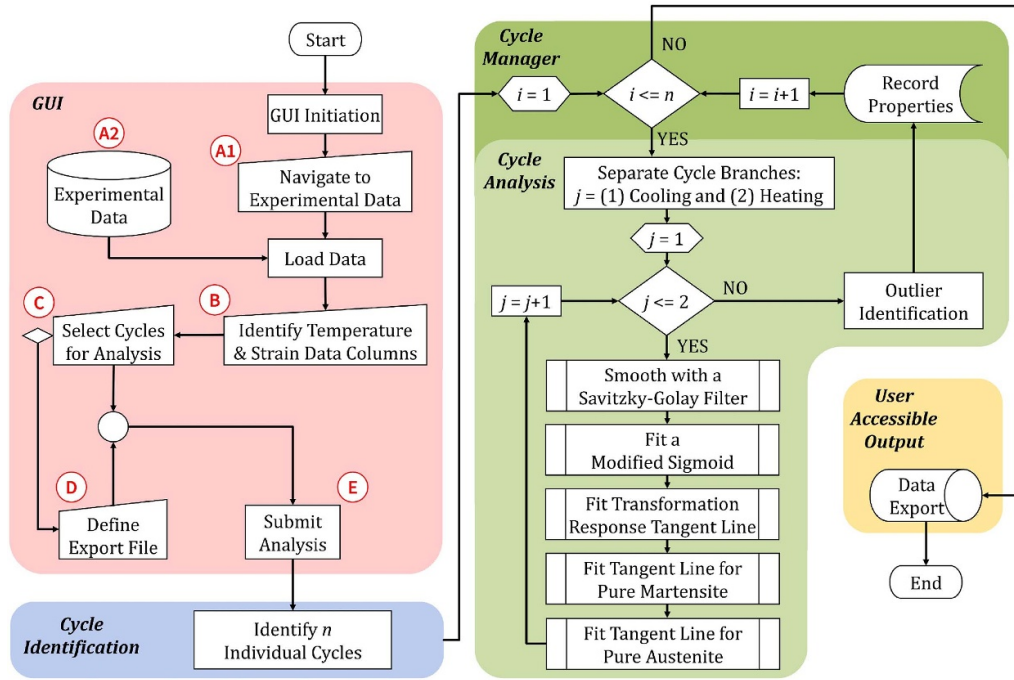


Figure 4. Flowchart of the processes employed by ASMADA.

- (b) by adjusting the values of the numerical spinboxes indicated by the 'B' field, the user is able to define which columns contain the temperature data and strain data. The adjacent dropdown menus allow the input of the units for each of the two fields. For the temperature units, three options are available ($^{\circ}\text{C}$, K, and $^{\circ}\text{F}$); for the strain units, two options are available (% and a dimensionless fraction). As the user changes the number ID of each column, the GUI highlights the specified columns in the preview table to help the user visualize their input.
- (c) from the dropdown menu indicated by 'C1', the user is able to either select analysis of all cycles included in the data set, or define in the input field 'C2' specific cycle ID number(s) and/or range(s) for analysis.
- (d) in field 'D' the name and format of the exported analysis results can be customized (optional).
- (e) SMA thermal cycling data analysis can be initiated, stopped, and reset by using the buttons highlighted in field 'E'.
- (f) the status bar denoted by field 'F' informs the user about the progress of data processing in real-time. This will also display detailed alerts for any user errors in data entry; errors encountered during analysis are displayed as well.

3.2. Pre-processing: cycle identification

After the raw temperature and strain data have been read according to the user input in the GUI, pre-processing can begin. Cycles are identified within the temperature data, wherein cycle cutoffs are determined as local temperature maxima using the `find_peaks` module within the SciPy library [53].

3.3. Cycle analysis

After cycles are identified, the following analysis process is iteratively performed on each specified cycle to determine the material properties and parameters previously listed in table 1. While all of these properties are calculated, this section focuses on determining the transformation start/finish points.

3.3.1. Branch separation. Each cycle is split into a cooling and a heating branch, with the cutoff determined as the minimum temperature value within a cycle.

3.3.2. Data smoothing. The cycle data is then smoothed using a Savitzky-Golay filter [54]. It is important to note that the cooling and heating rates employed in many experimental setups are different; hence, the branches of a cycle are smoothed 'separately'. The window sizes used for smoothing are determined as follows:

An array A is defined to contain the data either from a cooling or a heating cycle branch ('not' an entire cycle), as per equation (1). Array A is of size $r \times 2$, where r is the number of rows of (T, ε) data points in the cycle branch. Further, let $\lceil x \rceil$ denote a non-standard rounding function that rounds a value, x , to the nearest 'odd' integer.

$$A = \begin{bmatrix} T_1 & \varepsilon_1 \\ T_2 & \varepsilon_2 \\ \vdots & \vdots \\ T_r & \varepsilon_r \end{bmatrix}. \quad (1)$$

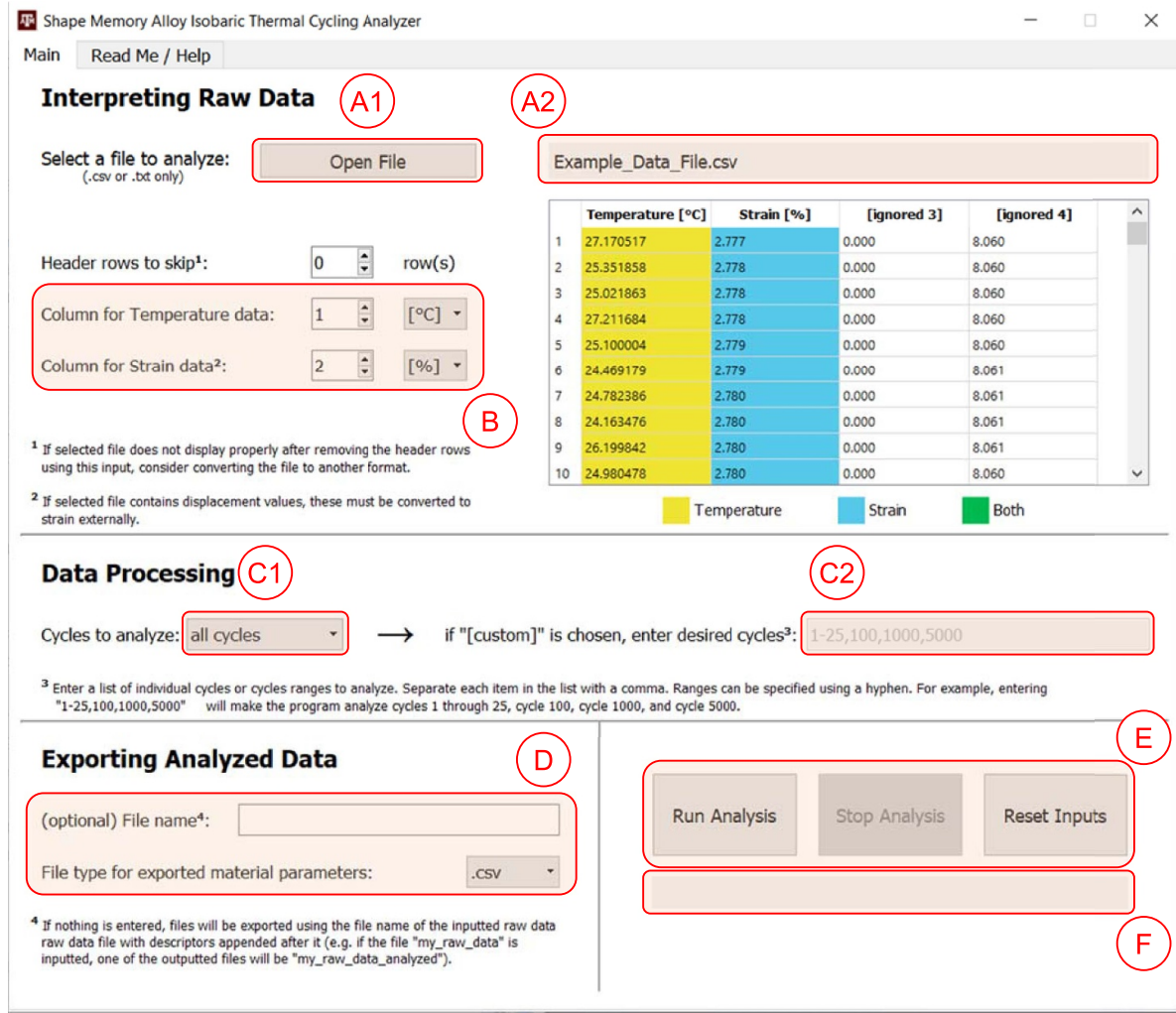


Figure 5. Graphical user interface with annotations on significant features.

For both temperature and strain data within a given branch, a window size of $\lceil \sqrt{r} \rceil$ was used when applying the Savitzky-Golay filter. Window sizes were made proportional to the square root of the number data rows, r , to account for different measurement frequencies employed by SMA researchers or imposed by the data acquisition equipment; in other words, this prevents the under-smoothing of experimental data collected at lower measurement frequencies, while also preventing over-smoothing of data collected at higher measurement frequencies (both of which would occur if a linear relationship between r and the filter window size was employed).

3.3.3. Finding tangent lines for transformation response regions. The process for determining the tangent line to the steeper transformation response region of each cycle branch involves fitting a modified sigmoid function, shown in equation (2), to the data. This is performed using the `curve_fit` module within the SciPy library [53].

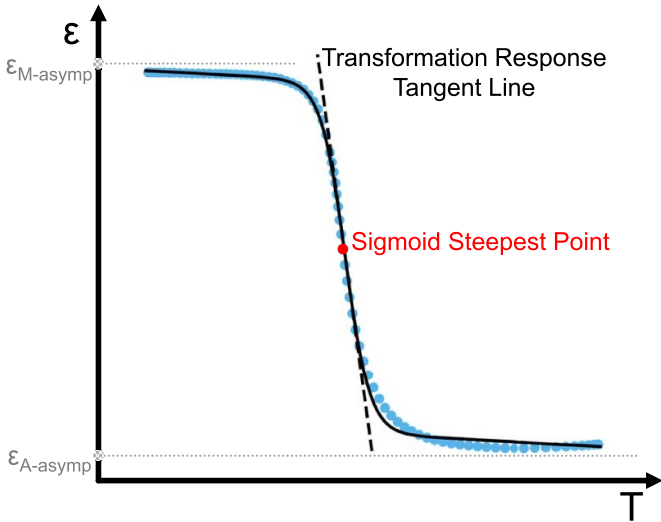
$$\varepsilon(T) = \varepsilon_{M-asympt} + \frac{\varepsilon_{A-asympt} - \varepsilon_{M-asympt}}{1 + |c| \exp(-b(T-d))} + mT. \quad (2)$$

In equation (2), $\varepsilon_{M-asympt}$ represents the strain value at the Martensite asymptote; $\varepsilon_{A-asympt}$ is the strain value at the Austenite asymptote; c and d are variables that control the strain and temperature of the central inflection point of the sigmoid, respectively; and b is the growth rate of the sigmoid. This functional form differs from a typical generalized sigmoid through the inclusion of a constant slope, m , that is applied; this constant slope allows the fitted function to more closely represent the experimental data, which would have a non-zero slope in single-phase regions due to thermal expansion. Bounds for these parameters are shown in table 2. For $\varepsilon_{A-asympt}$, $\varepsilon_{M-asympt}$, c , and d , the bounds are determined on a cycle-by-cycle basis to ensure the parameters stay close to the temperature/strain values observed in the cycle branch being analyzed. For b , the bounds were empirically selected to efficiently capture all data tested. For m , the bounds are set to physically comply with the known coefficients of thermal expansion exhibited by metal alloys.

The transformation response line is then determined as the line tangent to the fitted sigmoid at its steepest point (i.e. where the first derivative of strain with respect to temperature is at its maximum magnitude), as shown in figure 6. This process

Table 2. Bounds for parameters used to fit the modified sigmoids to the cycle branches. All strain values are unitless.

Parameter	Minimum	Maximum
$\varepsilon_{A-asympt}$	$\varepsilon_{cycle-min} - 0.05$	$\varepsilon_{cycle-max} + 0.05$
$\varepsilon_{M-asympt}$	$\varepsilon_{cycle-min} - 0.05$	$\varepsilon_{cycle-max} + 0.05$
b	0.001	10
c	$\varepsilon_{cycle-min}$	$\varepsilon_{cycle-max}$
d	LCT ($^{\circ}\text{C}$)	UCT ($^{\circ}\text{C}$)
m	$-1 \times 10^{-4} (^{\circ}\text{C}^{-1})$	$+1 \times 10^{-4} (^{\circ}\text{C}^{-1})$

**Figure 6.** Fitting of a modified sigmoid (solid black line) to experimental cooling branch data (blue) to determine the transformation response line (dashed black line).

is performed two times for each cycle: once for the cooling branch and once for the heating branch.

3.3.4. Finding tangent lines for pure phase regions.

Determination of the tangent lines to the single-phase regions involves a different process that is described herein. For the purposes of explanation, this section will focus on determining the line tangent to the fully Martensitic region that presents a linear response at the end of the cooling branch of a cycle. Similar methods are employed for the three other linearly approximated area at the beginning of the cooling branch, beginning of the heating branch, and at the end of the heating branch.

First, all points that could possibly be contained within the Martensitic region are identified. To do this, the intersection of two lines is employed: (a) the horizontal line $\varepsilon(T) = \varepsilon_{max-branch}$, where $\varepsilon_{max-branch}$ is the maximum strain value within the cycle branch; and (b) the transformation response line determined in section 3.3.3. The intersection point of these two lines defines a cutoff ('cross point'), where all the data located to the left of this critical value are deemed as 'candidate' data points to potentially use in the linear approximation of the pure Martensitic region. Next, the points corresponding to the lowest 50% of temperatures, i.e. the left-most

points (which fall between LCT and the 'end point') are isolated. Finally, a linear fit is applied to these left-most points, which serves as the approximation of the Martensite response line. Figure 7(a) presents a visual representation of this process; figure 7(b) shows the resulting Martensite response line for an example experimental cooling branch.

3.3.5. Determination of transformation start/finish points.

Transformation start/finish points are determined as the intersection of their respective transformation response lines and single-phase response lines, as shown in figure 8.

3.3.6. Identifying outliers.

Obtained transformation start/finish points are examined for outliers prior to exporting material properties to the user. Transformation temperatures that did not fall within the interval [LCT,UCT] were identified as outliers and made null. Transformation strains that did not fall within the interval $[\varepsilon_{cycle-min} - C, \varepsilon_{cycle-max} + C]$ are identified as outliers and made null. Note that strain outliers must be identified with the knowledge that it is possible for a transformation start/finish strain to be greater than the maximum or less than the minimum cycle strain (this occurs in cases in which the majority phase has a positive CTE); thus, an arbitrary constant, $C = 2$, was subtracted from the minimum/added to the maximum strains to define bounds for identifying outliers. Further note that both of these material properties are identified as potential outliers relative to the temperature and strain extrema 'in the cycle they were calculated from'; this method was chosen to account for changes in temperature and strain ranges over the course of ITC tests (most frequently seen in actuation fatigue tests).

After outliers have been removed from the data set, all material properties are exported as a '.csv' file type (unless specified otherwise by the user). A video is also exported to allow the user to visually inspect the accuracy of tangent line fitting for select cycles, alongside several figures of various material properties evolving with accumulating cycles.

The methods described in this section were implemented in Python, for which the source code has been made publicly available (see the Abstract or section 5); the efficacy of this implementation will now be described in the next section.

4. Results and discussion

ASMADA was used to analyze data from several different researchers within the field of SMA, including: the SMART group at Texas A&M University (USA) directed by Dr Dimitris Lagoudas, the MESAM group at Texas A&M University (USA) directed by Dr Ibrahim Karaman, Boeing Research & Technology (USA), and the SAAM group at the University of Patras (Greece) directed by Dr Dimitris Saravanos. The provided data was collected using a variety of experimental apparatuses (both commercial and in-house), testing methodologies, and material systems. For experimental apparatuses—temperature measurement equipment varied from infrared thermometers to contact thermocouples; strain measurement equipment varied from LVDT to axial extensometers to DIC;

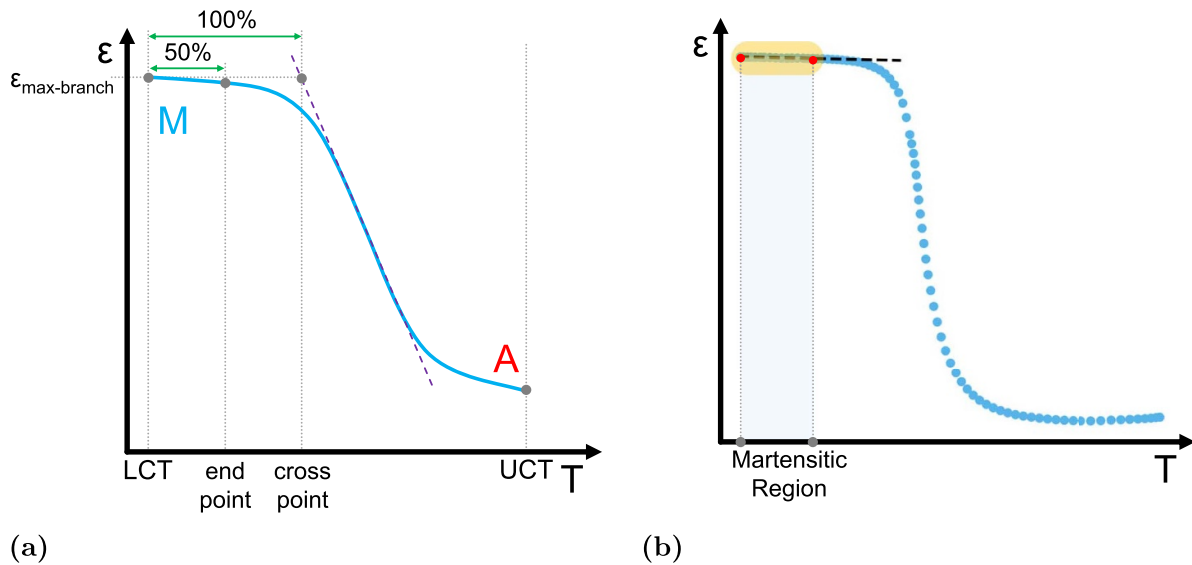


Figure 7. Fitting of a linear approximation for the pure phase response; (a) schematic demonstration of the method and (b) fitted line based on experimental data.

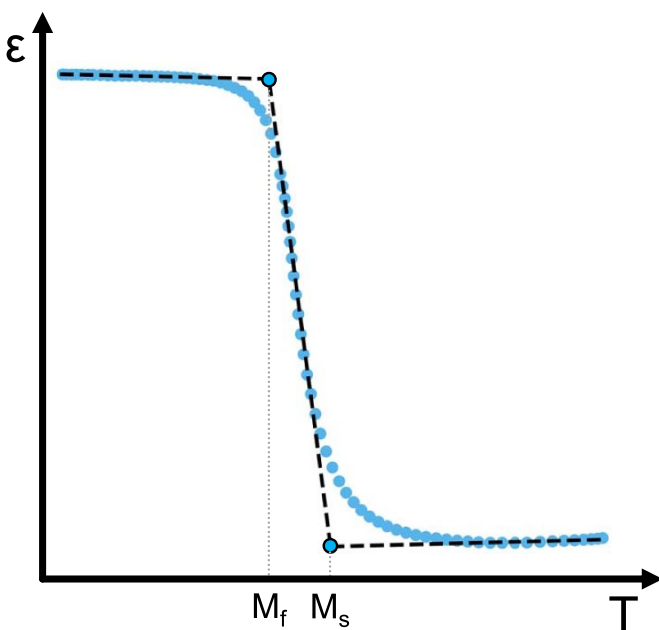


Figure 8. Determined transformation start/finish points for experimental cooling branch data.

cooling techniques varied from forced convection from a fan to forced convection using liquid nitrogen vapor; and heating techniques varied from Joule heating using both an AC and a DC power supply to induction heating and resistive heating ribbons. For experimental methodologies—application of stress included both uni-axial and shear stresses; tests were performed using both strain-control and temperature-control; for constant uni-axial stress tests, the applied load varied from 50 to 500 MPa; for constant shear stress tests, the applied torque varied from 12.5 to 75 N-m; heating and cooling rates

varied from 0.5 to 40 °C s⁻¹; and the frequency of data capture varied from 40 to 4500 points cycle⁻¹. Furthermore, data for several compositions of NiTi, NiTiHf, NiTiZr, and other SMA alloys were tested, wherein sample geometries included wires, ribbons, and dog-bones of varying dimensions. The aforementioned details suggest that the measuring frequencies, format and, of course, data itself capture a wide range of experimental configurations and measuring output.

In this section, we examine the robustness of the methods used to find transformation start/finish points, present plots depicting trends in several material properties over the course of an ITC test, detail the advantages and limitations of ASMADA, and identify future avenues of work.

4.1. Analysis demonstration

For the sake of simplicity, the focus of this section is on results from a single NiTiHf sample (kindly provided by Dr Karaman's group at Texas A&M University) which underwent actuation fatigue testing, referred to as the 'reference sample'. Additional data collected by other research groups using different experimental setups are analyzed and presented in the supplementary material accompanying this article. All results shown (figures, videos, and their underlying numerical data) were outputted directly from the tool, and have received no additional post-processing.

The reference sample underwent 2892 complete cycles prior to failure. Figure 9 shows the determination of transformation start/finish points for select cycles within the reference sample data; the tangent lines fitted to the single-phase and transformation response regions are shown. Cooling branch data are shown in blue, heating branch data are shown in red, tangent lines are shown as dashed black lines, and transformation start/finish points are shown in black. In the online version

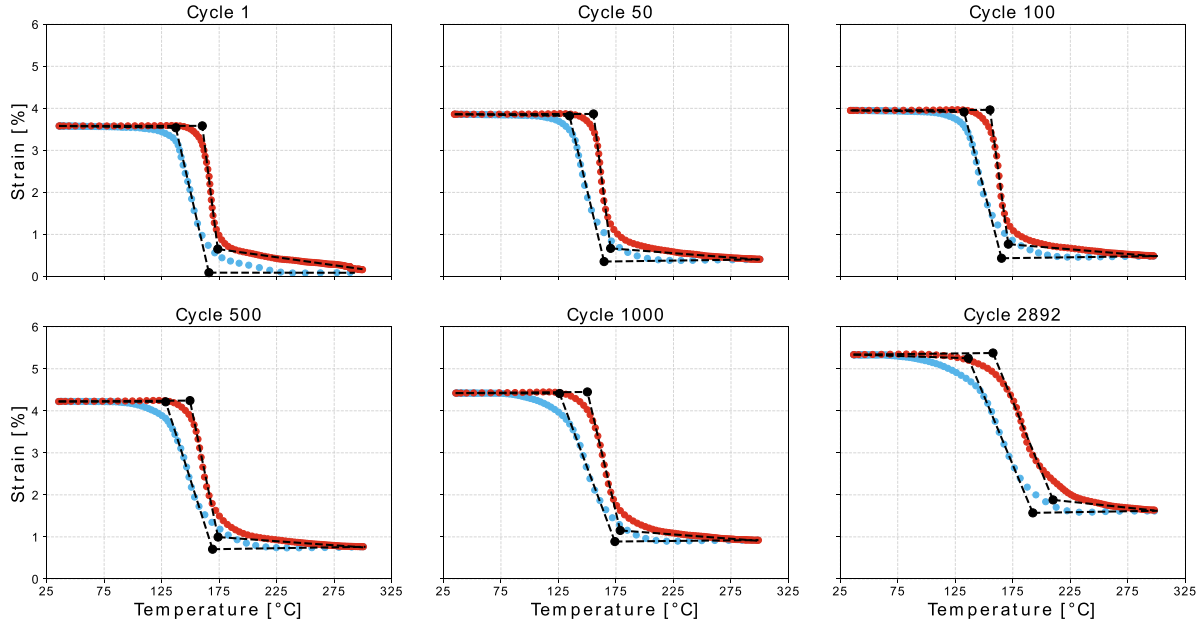


Figure 9. Determination of transformation start/finish points for select cycles within the reference sample.

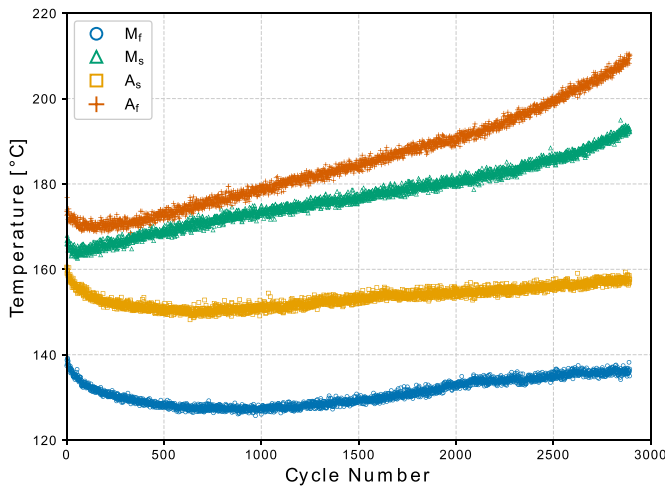


Figure 10. Evolution of transformation temperatures for the reference sample.

of the manuscript, this is shown in the form of a video, whereas the print version shows a static selection of cycles—the tool exports the video. A visual examination of the figure indicates consistent and reasonable determination of the transformation start/finish points.

The determined transformation start/finish temperatures are shown in figure 10. As can be seen, local deviations in the transformation temperatures are quite small ($\sim 3^\circ\text{C}$), implying the tool has a high degree of consistency. Further, this result elucidates a significant evolution of the transformation temperatures over the course of the reference sample's lifetime. For example, the Austenite finish temperature initially decreases over the first ~ 50 cycles; this is likely related to the

reorientation of Martensitic variants during the initial training of the sample. The A_f subsequently increases fairly linearly until failure. The net result is an increase in A_f by roughly 30°C . A similar trend is observed for the M_s temperature. Conversely, the M_f and A_s temperatures decrease more slowly and over a larger number of cycles; they subsequently increase less dramatically as well, resulting in little net change of these values at failure. Moreover, examining the trends in figure 10 (corresponding to NiTiHf) and figure S6 (corresponding to NiTiZr) from the supplementary material, the exhibited behavior of different alloy systems can be directly compared.

Figure 11 shows the (a) transformation strain and (b) actuation strain, alongside the corresponding values used to calculate these two properties. NiTiHf alloys are considered very stable in terms of their transformation response. As can be observed, the results reported in figure 11 indicate that the stroke length stays relatively constant for the reference sample, despite the development of residual TRIP strains. Interestingly, similar to figure 10, the likely effects of Martensitic variant reorientation during the initial training cycles can still be observed: ε_{A_s} , ε_{A_f} , ε_{LCT} , and ε_{UCT} all evolve more rapidly during the first ~ 50 cycles, after which their trends become relatively linear. Moreover, when comparing figure 11(a) to figures S7(a) and S11(a) from the supplementary material, it becomes evident that different SMA compositions present diverse trends. This is an interesting finding that could be further investigated using ASMADA by interested materials scientists and engineering researchers.

Figure 12 shows the residual strain evolution for the first 50 cycles of the reference sample. The asymptotically decreasing trend of the residual strain constitutes a typical SMA response to training, closely matching the qualitative diagram of figure 2(b).

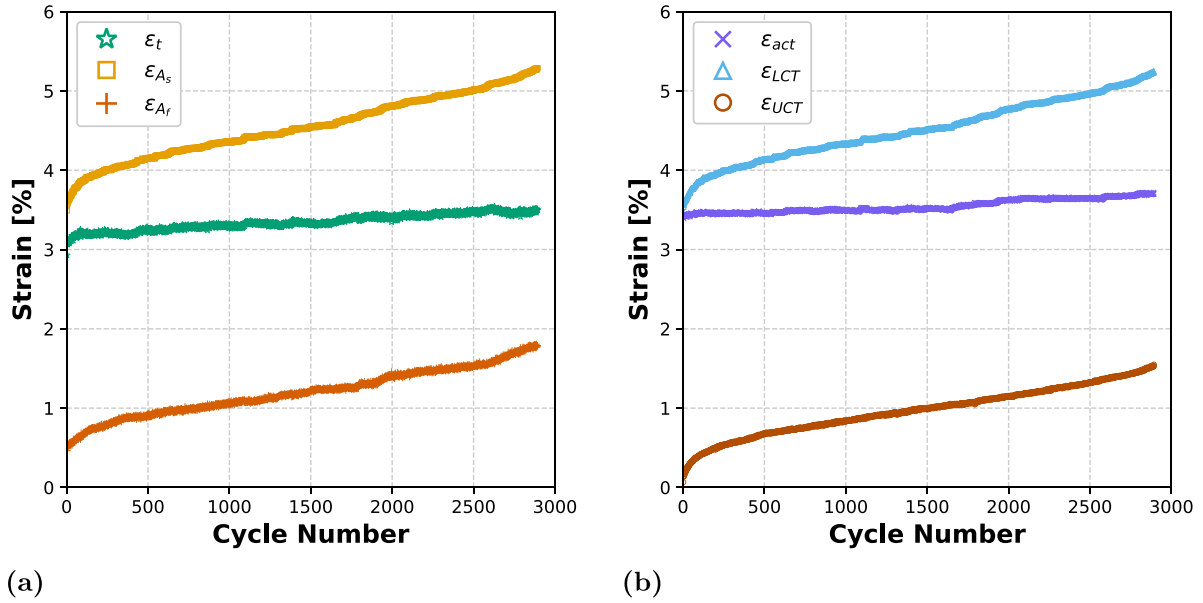


Figure 11. Evolution of the (a) transformation strain (ϵ_t) and (b) actuation strain (ϵ_{act}) for the reference sample.

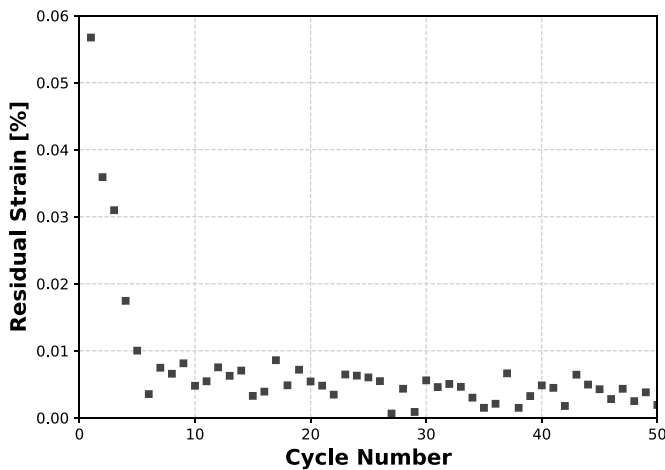


Figure 12. Evolution of residual strains for the reference sample. A moving average with window size 5 was applied to the presented data.

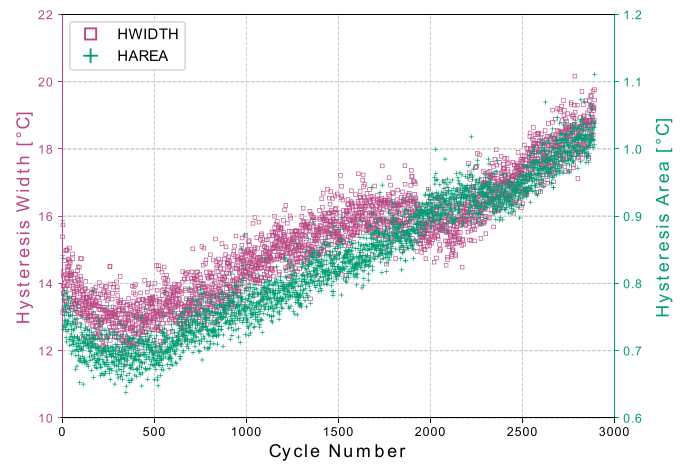


Figure 13. Evolution of the hysteresis width and hysteresis area for the reference sample.

Figure 13 presents the evolution of the hysteresis width (HWIDTH) and hysteresis area (HAREA). The trends in the evolutions of these properties appear strongly correlated. It is worth noting that local deviations in the HWIDTH are approximately the same as those for the transformation temperatures ($\sim 3^\circ\text{C}$); however, since HWIDTH is calculated as the difference between these transformation temperatures, HWIDTH assumes smaller values and thus the resultant variations are larger relative to the HWIDTH itself. It should also be noted that for HAREA (which has units equal to the product of the strain and temperature units), the strain component was converted from percent to dimensionless strain; HAREA can thus be converted to the specific energy of the thermal cycle by multiplying HAREA by the specific heat capacity of the material.

A list of all properties previously shown in table 1 are determined for each cycle and are exported by the tool. In addition to the figures shown here for the reference sample, several figures showing the evolution of other material properties and parameters are also exported.

4.2. Advantages of the proposed tool

The results obtained by ASMADA appear robust and consistent, as shown in section 4.1. To confirm this, the authors compared ASMADA's results with those obtained from manual analysis, as a standard benchmark does not exist. The authors manually analyzed 25 cycles from the reference sample (cycles 1, 100, 200, ..., 2400) and determined the four transformation temperatures for each cycle. The manually obtained results had an average relative error of 0.169% with a standard

deviation of 1.55%. On an absolute scale, the average error was $-0.118\text{ }^{\circ}\text{C}$ with a standard deviation of $2.35\text{ }^{\circ}\text{C}$. These error values demonstrate that ASMADA's calculations are comparable to those obtained via manual analysis, and thus are accurate relative to accepted methods.

Further, the analysis is very rapid compared with manual approaches that would require many labor hours or even days. Using ASMADA, the analysis of the reference sample ($n = 2892$ cycles) required $159 \pm 47\text{ s}$ (based on five test runs) when performed on a personal laptop computer (Intel i7-7700HQ CPU, 2.80 GHz). In comparison, the above manual analysis took approximately 96 min for only 25 cycles ($\sim 3.8\text{ min per cycle}$); to calculate all properties outputted by ASMADA, analysis time for the authors increased to $\sim 10\text{ min per cycle}$. Even assuming a generous manual analysis speed of 60 s cycle^{-1} , the manual process for all 2892 cycles would take $\sim 48\text{ h}$ of continuous labor. Hence, this tool allows researchers to study the evolution of many material properties, such as transformation start/finish temperatures, which was previously impractical due to the sluggish speed of manual analysis. It is important to highlight that the tool also removes any subjective interpretation of the data that arises during manual analysis.

Due to the ubiquitous nature of the methods used, alongside the user's ability to specify how to interpret their data using the developed GUI, this tool is able to analyze data collected for a wide variety of material systems and testing apparatuses. This allows for more thorough: (a) comparison of a research group's internal tests on a single material system to ensure consistency; (b) comparison of a research group's internal tests on different material systems; and (c) comparison of internal test results with those obtained by other research groups. Furthermore, the exported test parameters, such as the LCT and UCT for each cycle, allow researchers to more quantitatively identify issues in their testing apparatus/data acquisition techniques.

ASMADA has promise for modeling applications as well. For example, the implementation of machine learning (ML) is becoming prevalent throughout the scientific community. ML algorithms have previously been used to predict transformation temperatures [55] and hysteresis width [56] in new material systems based on limited existing data. However, a major roadblock to the further usage of ML for SMA applications is the lack of comprehensive, pointwise databases, as noted by Benafan *et al* [57]. The large volume of accurate data that is made accessible through this tool directly addresses this issue.

Finally, the proposed tool can be effectively used for the development and/or calibration of SMA constitutive models. For example, in the model of Lagoudas *et al* [22], the four transformation temperatures are obtained at different stress levels to define the phase diagram of the material and determine the values for key model parameters, such as the stress influence coefficient or Clapeyron slopes (C^A and C^M). The correlation of maximum transformation strain available with the uni-axial stress level through the H^{cur} function is derived based on experimental data that are output of ASMADA. Further, the transformation temperature thresholds are used in most constitutive models, such as the ones proposed by Buravalla and Khandelwal [58], Morin *et al* [59], Sedláč *et al*

[60], and Armattoo *et al* [61]. Moreover, providing the capability to report the evolution of critical temperature thresholds for the onset and completion of the transformation as well as the various strain quantities with the number of cycles allows for the development of proper constitutive equations that may account for associated phenomena, such as TRIP that has been investigated in the work of Xu *et al* [62]. Thus, the capabilities of ASMADA may also be leveraged beyond mere processing of SMA experimental data sets.

4.3. Limitations of the proposed tool

While ASMADA is able to analyze all of the data provided by the acknowledged researcher groups, the speed of analysis was shown to decrease for exceptionally large files. For samples below ~ 7500 cycles, the analysis was relatively efficient ($15\text{--}35\text{ cycles s}^{-1}$). For samples above ~ 7500 cycles, the analysis slowed down ($5\text{--}10\text{ cycles s}^{-1}$) – note that this is still significantly faster than manual analysis, and that analysis speeds are computer-dependent. Furthermore, the automated procedure for the analysis is performed individually for each file, rather than in batch.

The tool is not able to calculate all material properties for partially cycled samples. More specifically, transformation start/finish temperatures and strains are not all able to be determined (note that the authors are not aware of any ASTM standards pertaining to the analysis of partially cycled ITC samples). Properties such as LCT, ε_{LCT} , UCT, ε_{UCT} , ε_{res} , and ε_i , among others, are still captured.

Currently, ASMADA is only able to analyze iso-stress thermal cycling tests. Automatic analysis of pseudoelastic loading is not an offered capability of the tool in its current state, though this is a potential avenue for future work.

5. Summary

The ASMADA is presented. ASMADA is a tool for rapid, automatic analysis of SMA ITC test data. This primarily seeks to replace the time-consuming manual analysis of ITC test data, while simultaneously addressing the lack of well-defined analysis procedures contained in the relevant ASTM standard (E-3097-17). ASMADA implements a set of analysis procedures in open-source Python code, complete with a GUI for ease of use, and is now publicly available at <https://github.com/matthewkuner/ASMADA>. This tool:

- allows the user to quickly input how their data should be interpreted;
- automatically identifies thermal cycles within the data;
- applies pre-defined processes which determine twenty-three (23) material properties and parameters for each thermal cycle, including transformation start/finish temperatures; and
- exports these material properties.

To evaluate ASMADA, the tool was used to analyze a diverse set of ITC test data. The data examined was provided

by five researchers from four independent research groups, and was collected for several SMA alloys using a wide range of experimental techniques and apparatuses. The results obtained strongly demonstrate the robustness of this tool.

Data availability statement

The data generated and/or analysed during the current study are not publicly available for legal/ethical reasons but are available from the corresponding author on reasonable request.

Acknowledgments

The authors appreciate the insightful and stimulating discussions with Dr Ibrahim Karaman's team at Texas A&M University and more specifically Mr Alexander Demblon, Mr William Trehern and Ms. Carrie Jones, especially during the first steps of this work. The authors would also like to thank Mr Alexander Demblon, Dr Omer Karakoc, Mr James Mabe, Dr Robert Wheeler, and Dr Dimitris Saravanos for providing experimental data to test the automatic analysis tool. Furthermore, the authors would like to thank Dr Behrouz Haghgouyan for proofreading the manuscript. This research has been financially supported by the National Aeronautics and Space Administration (NASA) through the University Leadership Initiative (ULI) project under grant number NNX17AJ96A. The conclusions in this work are solely made by the authors and do not necessarily represent the perspectives of NASA.

ORCID iDs

Matthew C Kuner  <https://orcid.org/0000-0002-8218-8558>
Anargyros A Karakalas  <https://orcid.org/0000-0001-8528-9736>
Dimitris C Lagoudas  <https://orcid.org/0000-0002-0194-5933>

References

- [1] Benafan O, Moholt M R, Bass M, Mabe J H, Nicholson D E, Calkins F T 2019 *Shape Mem. Superelast.* **5** 415–428
- [2] Costanza G and Tata M E 2020 *Materials* **13** 1856
- [3] Bhardwaj A, Gupta A K, Padisala S K, Poluri K 2019 *Mater. Sci. Eng. C* **102** 730–42
- [4] Chillara V S C, Leon M H, Tsuruta R, Itakura E, Gandhi U and Dapino M J 2019 *J. Intell. Mater. Syst. Struct.* **30** 479–494
- [5] Asadpoori A, Keshavarzi A and Abedinzadeh R 2020 *Int. J. Crashworthiness* **26** 1–6
- [6] MacLean M and Farhat Z and Jarjoura G and Fayyad E and Abdullah A and Hassan M 2019 *Wear* **426–7** 265–76 22nd *International Conf. on Wear of Materials*
- [7] Lara-Quintanilla A, Hulskamp A W and Harald E N B 2013 *J. Intell. Mater. Syst. Struct.* **24** 1834–45
- [8] Karakalas A, Machairas T, Solomou A, Riziotis V, Saravanos D 2016 Development of SMA actuated morphing airfoil for wind turbine load alleviation *Proceedings of the TMS Middle East—Mediterranean Materials Congress on Energy and Infrastructure Systems (MEMA 2015)* ed I Karaman, R Arróyave, E Masad (Cham: Springer International Publishing) pp 181–90
- [9] Karakalas A A, Manolas D I, Machairas T T, Riziotis V A and Saravanos D A 2019 *Wind Energy* **22** 620–37
- [10] Lagoudas D C 2008 *Shape Memory Alloys: Modeling and Engineering Applications* 1st ed (US: Springer)
- [11] Calkins F T, Mabe J H, Butler G W 2006 Boeing's variable geometry chevron morphing aerospace structures for jet noise reduction smart structures and materials 2006: industrial and commercial applications of smart structures technologies vol 6171 ed E V White International Society for Optics and Photonics (SPIE) pp 199–210
- [12] Duerig TW, Melton K N, Stöckel D, Wayman C M 1990 *Engineering Aspects of Shape Memory Alloys* (Butterworth-Heinemann Ltd)
- [13] Otsuka K and Wayman C M 1998 *Shape Memory Materials* (Cambridge: Cambridge University Press)
- [14] Bigelow G S, Padula S A, Garg A, Gaydos D, Noebe R D 2010 *Metall. Mater. Trans. A* **41** 3065–79
- [15] Hebda D A and White S R 1995 *Smart Mater. Struct.* **4** 298–304
- [16] Schmidt M, Ullrich J, Wiecek A, Frenzel J, Schütze A, Eggeler G, Seelecke S 2015 *Shape Mem. Superelast.* **1** 132–41
- [17] Ansari M, Fahimi P, Baghani M and Golzar M 2018 *Int. J. Appl. Mech.* **10** 1850040
- [18] Calhoun C, Wheeler R, Baxevanis T, Lagoudas D C 2015 *Scr. Mater.* **95** 58–61
- [19] Mohajeri M, Behrouz H, Castaneda H and Lagoudas D C 2018 *Nickel Titanium Alloy Failure Analysis under Thermal Cycling and Mechanical Loading: A Preliminary Study* (NACE International) (available at: <https://onepetro.org/NACECORR/proceedings-abstract/CORR18/All-CORR18/NACE-2018-11632/126213>)
- [20] Karakoc O, Demblon A, Wheeler R W, Lagoudas D C, Karaman I 2019 Effects of testing parameters on the fatigue performance NiTiHf high temperature shape memory alloys *AIAA Scitech 2019 Forum* (available at: <https://arc.aiaa.org/action/showCitFormats?doi=10.2514/6.2019-0416>)
- [21] Jape S, Young B, Haghgouyan B, Hayrettin C, Baxevanis T, Lagoudas D C, Karaman I 2020 *Int. J. Solids Struct.* (<https://doi.org/10.1016/j.ijsolstr.2020.09.032>)
- [22] Lagoudas D, Hartl D, Chemisky Y, Machado L, Popov P 2012 *Int. J. Plast.* **32–3** 155–83
- [23] Saleeb A F, Dhakal B, Padula II S A and Gaydos D J 2013 *Smart Mater. Struct.* **22** 094017
- [24] Karakalas A A, Machairas T T, Solomou A G, Saravanos D A 2019 *Smart Mater. Struct.* **28** 035014
- [25] Karakoc O, Hayrettin C, Bass M, Wang S J, Canadinc D, Mabe J H, Lagoudas DC, Karaman I 2017 *Acta Mater.* **138** 185–97
- [26] Karakoc O, Hayrettin C, Evrigen A, Santamarta R, Canadinc D, Wheeler R W, Wang S J, Lagoudas D C, Karaman I 2019 *Acta Mater.* **175** 107–20
- [27] ASTM E3097-17 2017 Standard test method for mechanical uniaxial constant force thermal cycling of shape memory alloys *Technical Report* ASTM International West Conshohocken, PA
- [28] Hartl D J, Mooney J T, Lagoudas D C, Calkins F T and Mabe J H 2009 *Smart Mater. Struct.* **19** 015021
- [29] Sayyaadi H, Zakerzadeh M R, Salehi H 2012 *Sci. Iranica* **19** 249–57
- [30] Xue D, Yuan R, Zhou Y, Xue D, Lookman T, Zhang G, Ding X, Sun J 2016 *Sci. Rep.* **6** 28244
- [31] Saghaian S M, Karaca H E, Tobe H, Turabi A, Saedi S, Saghaian S, Chumlyakov Y, Noebe R 2017 *Acta Mater.* **134** 211–20

- [32] Duerig T W, Pelton A R, Bhattacharya K 2017 *Shape Mem. Superelast.* **3** 485–98
- [33] Benafan Othmane, Bigelow G S, and Wood L 2019 Ruggedness evaluation of ASTM international standard test methods for shape memory materials: E3097 standard test method for mechanical uniaxial constant force thermal cycling of shape memory alloys *Technical Report* National Aeronautics and Space Administration Glenn Research Center Cleveland, Ohio 44135
- [34] Kato H, Sasaki K 2021 *J. Mater. Sci.* **47** 1399–410
- [35] Kamyabi-Gol A, Herath D and Mendez P F 2017 *Can. Metall. Q.* **56** 85–93
- [36] Xiaojun Gu, Zhang Y, You Y, Xiaofei Ju, Zhu J, Moumni Z and Zhang W 2020 *Smart Mater. Struct.* **29** 095011
- [37] Karakoc O, Atli K, Evirgen A, Pons J, Santamarta R, Benafan O, Noebe R and Karaman I 2020 *Mater. Sci. Eng. A* **794** 139857
- [38] Bo Z, Lagoudas D C and Miller D 1999 *J. Eng. Mater. Technol.* **121** 75–85
- [39] Stebner A P et al 2014 *Acta Mater.* **76** 40–53
- [40] Tagiltsev A, Panchenko E, Chumlyakov Y, Fatkullin I and Karaman I 2020 *Mater. Lett.* **268** 127589
- [41] Hartl D J, Lagoudas D C, Calkins F T and Mabe J H 2010 *Smart Mater. Struct.* **19** 015020
- [42] Abuzaid W and Sehitoglu H 2017 *Mater. Sci. Eng. A* **696** 482–92
- [43] Sehitoglu H, Wu Y and Patriarca L 2017 *Scr. Mater.* **129** 11–5
- [44] Tagiltsev A I, Panchenko E Y, Timofeeva E, Chumlyakov Y I, Fatkullin I D, Marchenko E S and Karaman I 2021 *Smart Mater. Struct.* **30** 025039
- [45] Bucsek A N, Hudish G A, SBigelow G, Noebe R D and Stebner A P 2016 *Shape Mem. Superelast.* **2** 62–79
- [46] Chang S H, Lin P T and Tsai C W 2019 *Sci. Rep.* **9** 19598
- [47] Chen C H and Chen Y J 2019 *Scr. Mater.* **162** 185–9
- [48] Matsuda H, Shimojo M, Murakami H and Yamabe-Mitarai Y 2021 Martensitic transformation of high-entropy and medium-entropy shape memory alloys *THERMEC 2021 (Materials Science Forum)* vol 1016 (Trans Tech Publications Ltd) pp 1802–10
- [49] Peltier L, Lohmuller P, Meraghni F, Berveiller S, Patoor E and Laheurte P 2020 *Shape Mem. Superelast.* **6** 273–83
- [50] Monteiro P C C, da Silva Monteiro L L, Savi M A, Netto T A, Pacheco P M and de Paiva T 2017 *J. Intell. Mater. Syst. Struct.* **28** 1415–1427
- [51] Bhattacharya K 1992 *Arch. Ration. Mech. Anal.* **120** 201–44
- [52] ASTM F2005-05 (2015) 2015 Standard terminology for nickel-titanium shape memory alloys *Technical Report* ASTM International West Conshohocken, PA
- [53] Virtanen P et al 2020 *Nat. Methods* **17** 261–272
- [54] Savitzky A, Golay M J E 1964 *Anal. Chem.* **36** 1627–39
- [55] Xue D, Xue D, Yuan R, Zhou Y, Balachandran P V, Ding X, Sun J and Lookman T 2017 *Acta Mater.* **125** 532–541
- [56] Xue D, Balachandran P V, Hogden J, Theiler J, Xue D and Lookman T 2016 *Nat. Commun.* **7** 11241
- [57] Benafan O, Bigelow G S and Young A W 2020 *Adv. Eng. Mater.* **22** 1901370
- [58] Buravalla V and Khandelwal A 2008 *AIP Conf. Proc.* **1029** 104–123
- [59] Morin C, Moumni Z and Zaki W 2011 *Int. J. Plast* **27** 748–67
- [60] Sedlák P, Frost M, Benešová B, Ben Zineb T and Šittner P 2012 *Int. J. Plast* **39** 132–151
- [61] Armattoe K, Bouby C, Haboussi M and Ben Z T 2016 *Int. J. Solids Struct.* **88** 283–95
- [62] Xu L, Solomou A, Baxevanis T and Lagoudas D C 2019 A three-dimensional constitutive modeling for shape memory alloys considering two-way shape memory effect and transformation-induced plasticity *AIAA Scitech 2019 Forum* (Reston, Virginia: American Institute of Aeronautics and Astronautics)